


Stacking-dependent anomalous valley Hall effect in bilayer Janus VSCI

Rui-Chuan Zhang and Hai-Yuan Chen ^{*}*School of Materials and Energy, University of Electronic Science and Technology of China, Chengdu 610054, China*

(Received 11 July 2023; accepted 8 August 2023; published 21 August 2023)

H-phase hexagonal two-dimensional lattices have been extensively studied in the field of valleytronics. In contrast, their counterparts in the T phase have received relatively less attention due to the presence of inversion symmetry, which limits the potential for generating an anomalous valley Hall effect (AVHE). However, the Janus and bilayer stacking structures provide additional prospects to discover extra candidates. Herein, we employed first-principles calculations to predict the stacking-dependent AVHE in bilayer Janus VSCI. Owing to the intrinsic net magnetic moment, the valleys of the monolayer Janus VSCI are spontaneously polarized by out-of-plane magnetization, obviating the need for the external magnetic substrate. This valley polarization can be maintained through specific stacking configurations, allowing electrons with identical spins but different valley indices to flow toward the same side, which results in a significant AVHE and the emergence of a spin current. Notably, we found that interlayer coupling can selectively enhance or diminish the Berry curvatures of the two nonequivalent valleys, even without any external strain. Additionally, the results are effectively explicable through the analysis of our proposed model. In this paper, we present a promising material and put forth ideas for uncovering valleytronic candidates.

DOI: [10.1103/PhysRevB.108.075423](https://doi.org/10.1103/PhysRevB.108.075423)

I. INTRODUCTION

Valleytronics has rapidly emerged as an advancing field with enormous potential for the development of informatic devices and logic processors [1,2]. The appearance of the valley provides practical applications with an additional degree of freedom (DOF) that mainly exists in two-dimensional (2D) materials. These valleys are located at the corners of the Brillouin zone (BZ) and represent the extreme energy levels of the band dispersion [3,4]. However, manipulating and generating valley polarization by lifting the degeneracy between the $+K$ and $-K$ valleys remains a challenge for the development of valleytronic devices. This is where 2D ferromagnetic (FM) semiconductors come in—offering an unprecedented opportunity for quantum control of the valley index [5–8]. Meanwhile, the valley Hall effect in ferrovalley materials possesses an attractive feature: the presence of additional charge Hall current originating from the spontaneous valley polarization [9], known as the anomalous valley Hall effect (AVHE). The AVHE based on valley DOF has been extensively studied in 2D hexagonal materials [10,11]. However, for real applications, a large valley polarization difference is highly desirable to avoid the impact of thermal noise on valleytronic devices.

Currently, there are numerous approaches employed for achieving valley polarization, including optical pumping [12], magnetic field manipulation [13–15], magnetic substrates supporting [16–18], and magnetic doping [19,20]. However, each of these techniques presents certain limitations. For instance, optical pumping and the application of a magnetic field are known to exhibit volatility, while the use of magnetic

substrates or carrier doping can disrupt the intrinsic band structures of valley materials [21]. Consequently, the quest for materials that exhibit spontaneous valley polarization assumes significant importance in the realm of AVHE research. Authors of early reports mainly concentrated on the monolayer H-phase lattice due to its broken inversion symmetry (IS) and better stability generally compared with the T-phase counterpart [22–25]. Moreover, bilayer stacking can pose challenges to maintaining IS and thus may not be the preferred strategy. Fortunately, recent approaches that involve constraints imposed on crystalline symmetry have paved the way for a specific coupling between layers. This yields the realization of valley-contrasting linear dichroism, optical selection of the valley, and polarization of interlayer excitons, even with the proposal of the layer-polarized anomalous Hall effect (LP-AHE) [26–28]. Nonetheless, authors of few works have considered the intrinsic valley polarization in bilayer systems stacking by T-phase monolayers [29–32]. Bilayer T-FeCl₂ exhibited a valley polarization of 5.3 meV, where van der Waals interaction is introduced through constructing a bilayer lattice [33]. However, the small valley polarization still largely restricts its application. To address this issue, the occurrence of Janus transition metal dichalcogenides (TMDs) has provided a platform and strategy to investigate the effect of interlayer coupling on valley polarization and design feasible materials [34,35]. Janus materials are currently becoming more and more attractive in spintronics, as evidenced by previous researchers discussing their potential to realize skyrmion states and Dzyaloshinskii-Moriya interaction (DMI) [36,37]. In this context, it is particularly interesting to explore their applications in valleytronics. By considering the monolayer Janus structure without IS, considerable work has been carried out to study the valley polarization [38–41]. Interestingly, unlike H-phase Janus VXY ($X = \text{Cl, Br, I}$; $Y = \text{S, Se, Te}$)

^{*}hychen@uestc.edu.cn

with no magnetic moments [42], the monolayer T-phase Janus VSCI is an inherently FM semiconductor with a Curie temperature of 125 K [43]. The significance of Janus bilayers, as compared with monolayers, lies in their concentrated Berry curvature at the K points, resulting in a more pronounced and pure valley Hall effect. Additionally, Janus bilayers exhibit prolonged persistence of valley excitons from the same valley but different layers, surpassing the temporal limitations observed in single-layer structures. These benefits will be thoroughly discussed. Therefore, we are curious about the stacking-dependent valley polarization in such a Janus bilayer system.

To find the answer, steered via first-principles calculations, bilayer stacking models are proposed to discover the stacking-dependent AVHE in bilayer Janus VSCI. All stacking configurations behave as FM semiconductors with band edges located at the $+K/-K$ points, giving rise to valley-dependent physics. As a result, both the band gaps and valley polarizations are sizeable, suggesting that bilayer VSCI can be applied to information storage devices. More intriguingly, the valley polarization can be almost completely inherited from the monolayer due to the large band-edge energy difference between two layers, which is conventionally achieved by an external electric field [30]. Furthermore, we analyzed the effect of different stacking models on the Berry curvature by applying the two-band model considering the valley polarization. In this paper, we reveal that bilayer Janus VSCI is a promising candidate for valleytronic applications.

II. METHOD

First-principles calculations were performed based on density functional theory with the projector augmented-wave method as implemented in VASP [44–46]. The exchange-correlation interactions were treated by generalized gradient approximation (GGA) in the form of the Perdew-Burke-Ernzerhof functional [47]. The cutoff energy of the plane-wave basis was set to 520 eV. To avoid interactions between adjacent layers, the vacuum space was set to 20 Å. In addition, the van der Waals corrections were included as parametrized in the semiempirical DFT-D3 method [48]. A $5 \times 5 \times 1$ K -point mesh was used to sample the 2D BZ to determine the most stable magnetization type and the optimal stacking configurations. A Γ -centered $11 \times 11 \times 1$ mesh was used for further lattice relaxation and the following steps. The force convergence criterion was set to 0.01 eV/Å, and the convergence criterion of the total energy was set to 10^{-5} eV. To better describe the strong correlation effect for the localized $3d$ electrons of V atoms, the GGA+ U method was considered [$U_{\text{eff}} = (U - J) = 2.0$ eV] [43]. The Heyd-Scuseria-Ernzerhof (HSE) hybrid functional was employed for comparison [49]. The spin-orbit coupling (SOC) effect was included in the calculation of the band structures. The stacking energy and magnetic anisotropy energy (MAE) computations were conducted with the help of the VASPKIT package [50]. Berry curvatures were computed by employing the VASPBERRY package [51], and the anomalous Hall conductivity was computed by implementing the maximally localized Wannier functions in the WANNIER90 package [52].

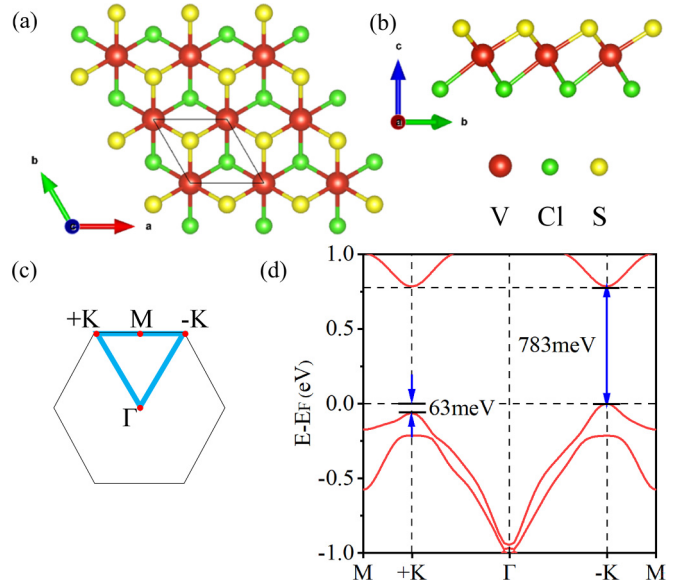


FIG. 1. (a) Top and (b) side views of the crystal structure of monolayer Janus VSCI. (c) Two-dimensional (2D) Brillouin zone (BZ) marked with the high-symmetry k points and path. (d) The band structure of the single-layer VSCI (GGA + U + SOC) with the Fermi level set to 0 eV.

III. RESULTS AND DISCUSSION

Figures 1(a) and 1(b) show the structure of monolayer Janus VSCI, which appears to be a hexagonal lattice with the space group of $P3m1$. Like the T-phase TMDs with octahedral coordination [53], in monolayer Janus VSCI, the upper and lower surfaces are occupied by chlorine and sulfur atoms, respectively, sandwiching the transition metal in the middle. Because of this unique arrangement, monolayer Janus VSCI exhibits the intrinsic broken IS. The magnetic moment per unit cell is computed to be $2 \mu_B$, which is consistent with the previous study [43]. Figure 1(c) shows the high-symmetry k points and the selected path in the first BZ, which displays the two nonequivalent valleys, namely, $+K$ and $-K$. The band structure of single-layer VSCI is illustrated in Fig. 1(d), with considerable energy splitting between the valleys.

When stacking two single layers, three different interlayer terminations including Cl-S, S-S, and Cl-Cl are considered. Additionally, direct stacking (D) like AA-type in bilayer TMDs and the inverse stacking (I) by flipping the top layer are also included [54]. Therefore, six stacking configurations are initially constructed for searching the ground states, as shown in the Supplemental Material [55]. To screen the most stable magnetization type and optimal stacking site for each configuration, the corresponding energies are computed for each model sliding along the 2D grids shown in Fig. 2. The operations involve fixing the bottom layer and sliding the top layer throughout the entire unit cell region, followed by relaxing the lattice for FM and antiferromagnetic (AFM) cases to obtain the ground state energies. Interestingly, all the stable stacking models have FM ground states. It is intriguing to discover that, for direct stackings, the lowest-energy states are all shift free, as the minimum values of the diagrams are all at the origins of coordinates, while for

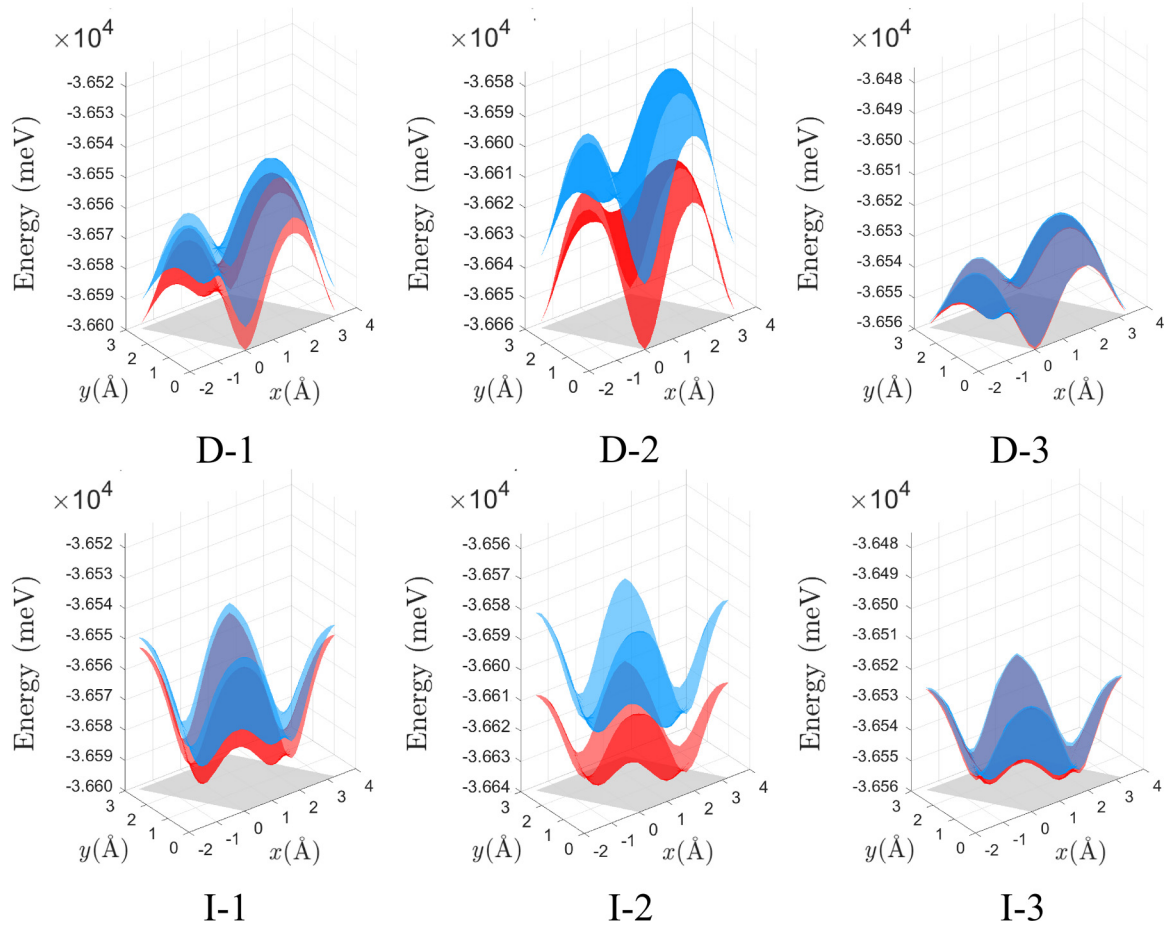


FIG. 2. The stacking energy associated with the ferromagnetic (FM) state depicted in red and the antiferromagnetic (AFM) state depicted in blue for each stacking configuration. The projection onto the xOy plane represents the range of sliding vectors, which corresponds to the size of the unit cell.

inverse stackings, the lowest-energy states are all characterized by a sliding displacement of $(\frac{1}{3}, \frac{2}{3})$. All stacking types tend to be FM coupling, given that the energy levels of the FM states are lower than those of the AFM states, regardless of the configurations. More interestingly, the stacking energy differences between FM and AFM are most pronounced in D-2 and I-2 types, while D-3 and I-3 are almost equivalent. This indicates that the atomic types of interlayer coupling affect the magnetic stability, i.e., the ease of transitioning from FM to AFM. In addition, it should be noted that the diagrams of I-2 and I-3 demonstrate diagonal mirror symmetry. This characteristic arises since the two distinct stacking

configurations associated with the symmetrical points on the graph exhibit enantiomeric chirality. The structures of the optimized configurations with FM states and optimal stacking sites are shown in Fig. 3. To confirm the dynamic stability of each stacking configuration, the phonon spectra were illustrated (see Supplemental Material [55]) to exhibit the absence of imaginary frequencies in the whole BZ [56].

Based on the above stable configurations, we further compute the MAE to ascertain the most favorable magnetization direction. Figure 4 illustrates the orientation that facilitates the most accessible magnetization and the corresponding extreme values of MAE. Obviously, all stacking configurations

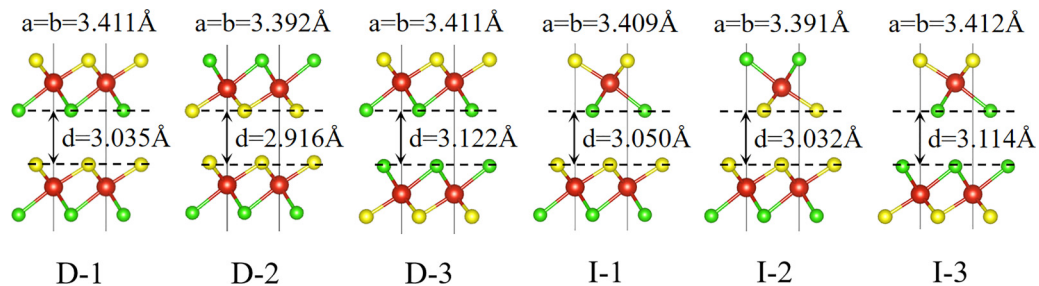


FIG. 3. Side view of six stacking configurations after optimization with the lattice parameters and interlayer distances.

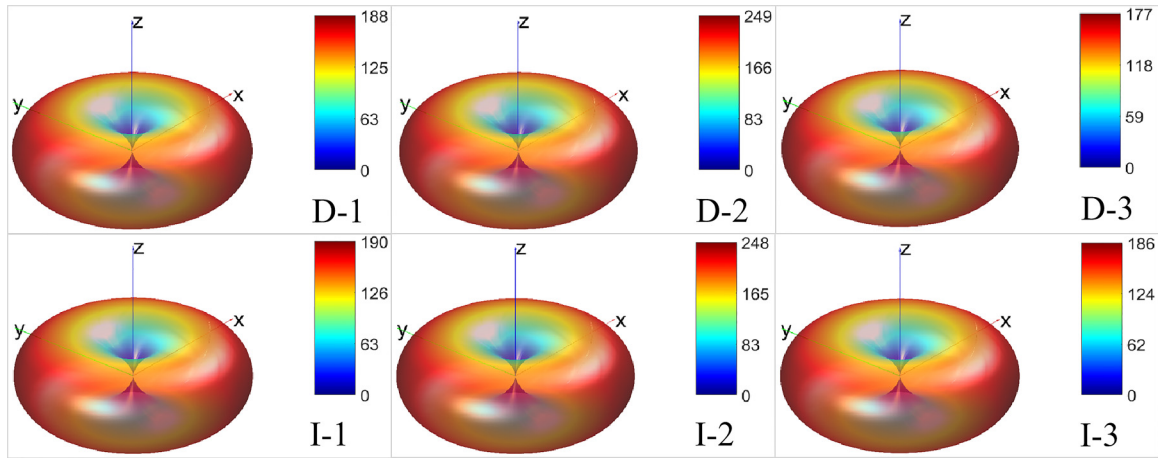


FIG. 4. Spherical plot of magnetic anisotropy energy (MAE) arises from rotating the spin axis from the easy axis of each stacking configuration (units: μeV). The MAE is set to zero in the out-of-plane direction.

favor out-of-plane magnetization, which arises from perpendicular magnetic anisotropy (PMA). Distinct from VSi_2N_4 , the VSCI monolayer demonstrates inherent PMA without requiring external strain and surpasses the MAE of the previously documented VSe_2 monolayer ($\sim 150\mu\text{eV}$) [57,58]. This property has been extensively investigated in the field of spintronics due to its potential for scalable magnetic random-access memories [59]. Beyond this, FM bilayers have shown

even broader applicability, as evidenced by their utilization in various devices such as self-rotating torque and self-transfer torque devices, as reported previously [60,61]. The angular dependence of MAE is determined by the symmetry of the crystal structure, which can be described by $E(\theta) = K_1^{\text{eff}}\sin^2\theta + K_2\sin^4\theta$. After fitting the results, it is found that the extreme value corresponding to the in-plane magnetization is K_1^{eff} , i.e., the maximum value of the color bar in Fig. 4

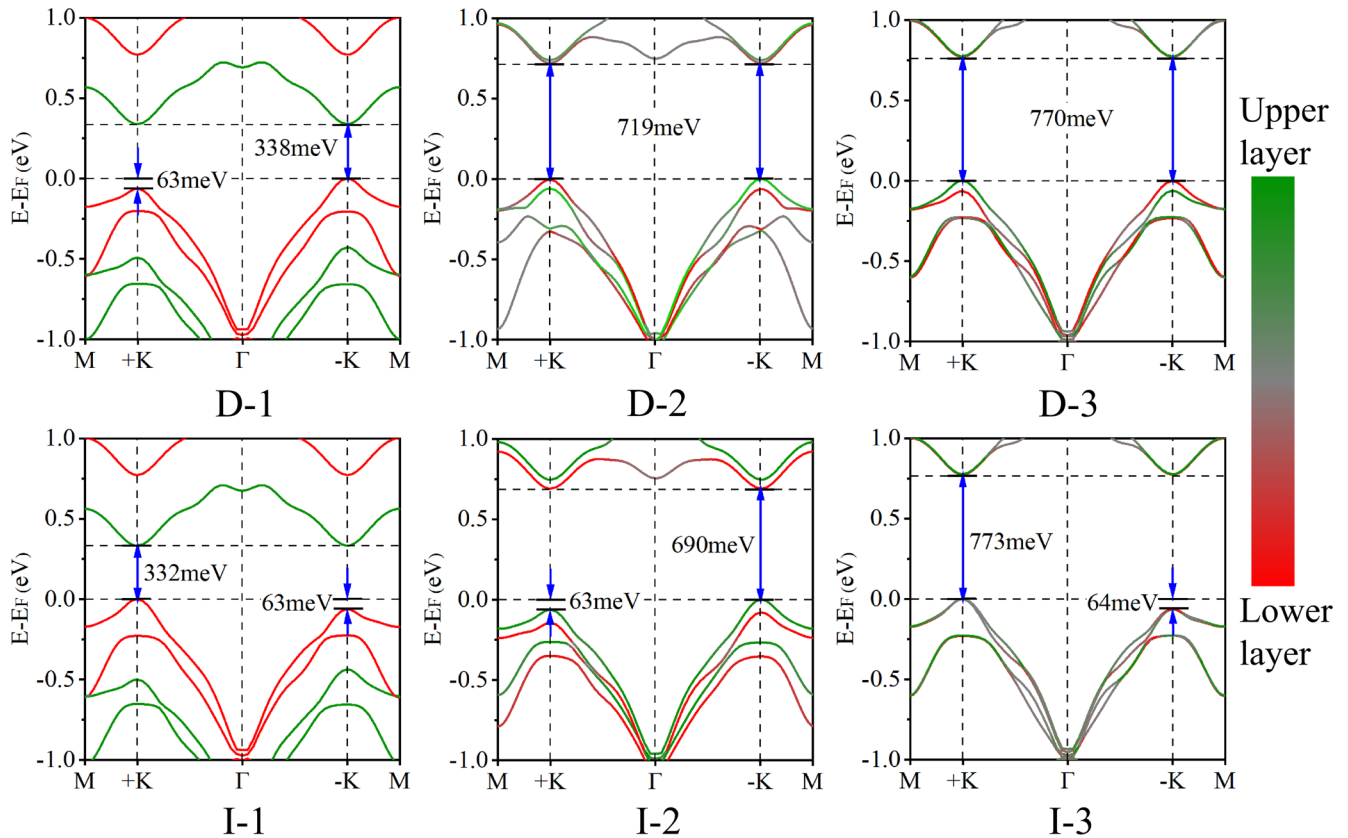


FIG. 5. Band structures of each stacking configuration (GGA + U + SOC) with the Fermi level set to 0 eV. The color gradient indicates contributions from different layers to the band, where green represents contributions from upper layers and red represents contributions from lower layers.

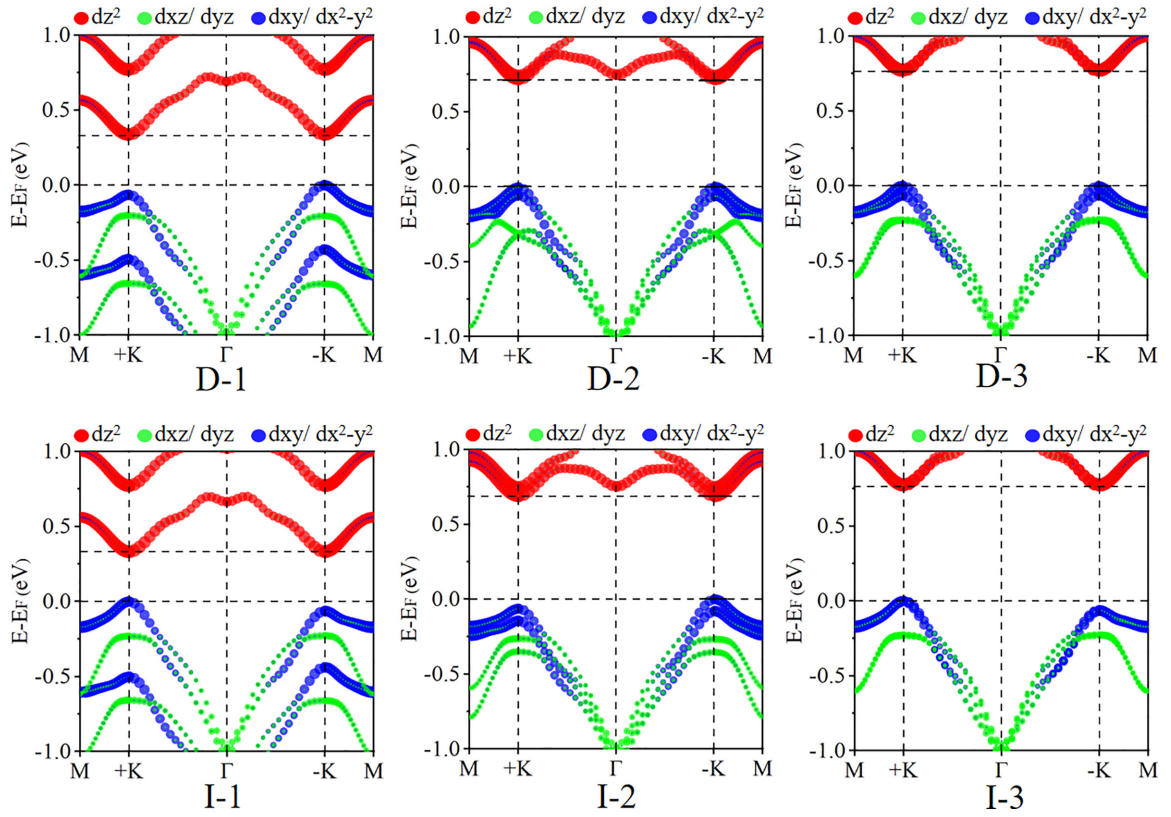


FIG. 6. Orbital-resolved band structures of each stacking configuration with the red, green, and blue dots representing the contribution from d_{z^2} , d_{xz}/d_{yz} , and $d_{xy}/d_{x^2-y^2}$ orbitals, respectively.

(ranging from 177 to 249), while $K_2 \sim 0$. This ensures that all the configurations fall under the category of out-of-plane magnetization type [59].

After discussing the structure and magnetization, Fig. 5 presents the band structures of each stacking configuration with their respective Fermi energy subtracted. It turns out that all stacked configurations are semiconductors with valence band maximum (VBM) and conduction band minimum (CBM) both located at the $+K/-K$ points. The band gaps of D-1 and I-1 are significantly reduced compared with the single layer due to a considerable band-edge energy difference between the upper and lower layers, while other configurations exhibit band gaps ≥ 690 meV, with a negligible band-edge energy difference. As for valley exciton physics, the persistence of excitons with valley-specific characteristics originating from the same valley but different layers would be significantly prolonged, as is the case in the first stacking type, exceeding the possible duration in a single layer. This phenomenon presents a potential avenue for inquiry and applications in the field of information [62]. Additionally, it was observed in a previous study on general TMDs that an applied electric field was required to achieve the band-edge energy difference between two coupled layers [30]. However, the materials designed in this paper, namely, I-1 and D-1, exhibit intrinsic band-edge energy differences, which will be further discussed later. Additionally, D-1 and all inverse stacking configurations exhibit large valley polarization, which is made even more significant in the HSE band structures up to ~ 70 meV (shown in the Supplemental

Material [55]), suggesting the potential for their application as relatively high-temperature semiconductors. Since the most stable states of shift-free D-2 and D-3 possess intrinsic IS, the valley polarization vanishes. This indicates that the two degenerate valence band tops at the $+K/-K$ valleys can be considered as contributions from two different V atoms.

The generation of valley polarization relies on the combined influence of magnetism and SOC. Magnetism removes spin degeneracy in energy, while SOC distinguishes spin states in momentum space. To explore the cause of the discrepancy at $+K/-K$ valleys, the orbital-resolved band structures are shown in Fig. 6, from which it is obvious that the bottom of the conduction band and the top of the valence band are predominantly contributed by d_{z^2} and $d_{x^2-y^2}/d_{xy}$ orbitals, respectively. Moreover, the tight-binding model was used to approximate the treatment, neglecting the effect of interlayer coupling and treating the hybridized orbitals as the orbitals of individual atoms. For FM material, considering the states around the Fermi level are from the same spin channel, the Hamiltonian for SOC can be expressed as [63,64]

$$\hat{H}_{\text{SOC}} = \lambda \hat{S}_z (\hat{L}_z \cos \theta + \frac{1}{2} \hat{L}_+ e^{-i\phi} \sin \theta + \frac{1}{2} \hat{L}_- e^{+i\phi} \sin \theta). \quad (1)$$

When the magnetization orientation is along the z axis, $\theta = 0$; thus, we have

$$\hat{H}_{\text{SOC}} = \lambda \hat{S}_z \hat{L}_z. \quad (2)$$

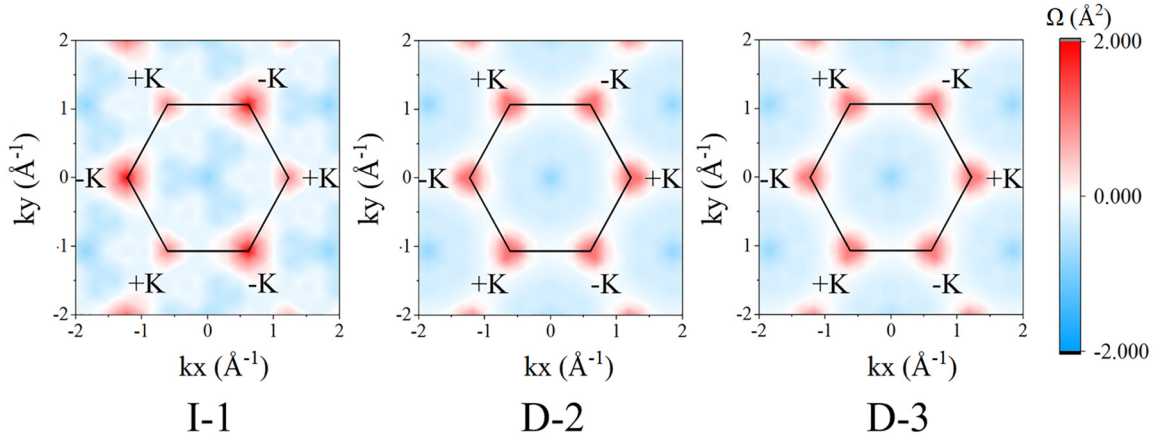


FIG. 7. Berry curvatures of I-1, D-2, and D-3 as a countermap over the two-dimensional (2D) Brillouin zone (BZ) obtained by the Kubo formula approach.

Considering the orbital contribution around the valleys and the C_3 symmetry, the basis functions of conduction and valence bands can be chosen as

$$|\psi_c\rangle = |d_{z^2}\rangle, \quad (3)$$

$$|\psi_v\rangle = \sqrt{\frac{1}{2}}(|d_{x^2-y^2}\rangle + i\tau|d_{xy}\rangle), \quad \tau = \pm 1, \quad (4)$$

where c/v indicates the conduction/valence band, and τ represents the valley index. The energy levels of the $+K/-K$ valleys can be written as

$$E_c = \langle \psi_c | \hat{H}_{\text{SOC}} | \psi_c \rangle, \quad (5)$$

$$E_v = \langle \psi_v | \hat{H}_{\text{SOC}} | \psi_v \rangle. \quad (6)$$

As a result, the valley band-edge energy differences in both conduction and valence bands can be written as

$$\Delta E_c = E_c^{+k} - E_c^{-k} = 0, \quad (7)$$

$$\begin{aligned} \Delta E_v &= E_v^{+k} - E_v^{-k} = i\langle d_{x^2-y^2} | \hat{H}_{\text{SOC}} | d_{xy} \rangle - i\langle d_{xy} | \hat{H}_{\text{SOC}} | d_{x^2-y^2} \rangle \\ &= 4\lambda\hbar\langle d_x^2 - y^2 | \hat{S}_z | d_{x^2-y^2} \rangle = 2\lambda\hbar^2. \end{aligned} \quad (8)$$

Here, we used $\hat{L}_z |d_{z^2}\rangle = 0$, $\hat{L}_z |d_{x^2-y^2}\rangle = 2i\hbar |d_{xy}\rangle$. These explanations clarify why there is little splitting in the conduction band, while in the valence band, the splitting is pronounced. Here, since the interlayer hopping is inappreciable compared with the intralayer ones, the van der Waals interaction only causes a loose coupling. Therefore, the behavior of electrons in the bilayer can be roughly described by the superposition of band structures for two unstacked single layers. The symmetry operation results in the cross-superposition of K valleys in I-1, D-2, and D-3. In this case, the $+K$ valley of the upper layer overlaps with the $-K$ valley of the lower layer to form the same K valley in the bilayer. On the contrary, the other valley in the bilayer is composed of the respective antithesis of the single layers. Hence, for the upper and lower layers, the valence band features contrasting relative heights in the K valleys. Additionally, due to the significant band-edge energy difference between the two single layers in I-1, it is unconventional that the valley polarization is almost

completely preserved even when the two K valleys are cross-superimposed, making it a unique and intriguing property of the Janus structure.

Along with the band structure, when the K valleys are cross-superimposed, the positive and negative peaks in the Berry curvature of the coupled single layers cancel each other out, resulting in a net value that represents the Berry curvature of the bilayer. According to the semiclassical dynamics of the wave packet, the group velocity can be expressed as [65]

$$\dot{\vec{r}} = \frac{1}{\hbar} \frac{\partial \tilde{E}_{\vec{k}}}{\partial \vec{k}} - \dot{\vec{k}} \times \tilde{\Omega}, \quad (9)$$

with the second term denoting the anomalous velocity, which is directly proportional to the magnitude of the Berry curvature since the Berry curvature can be regarded as the magnetic field in reciprocal space. Meanwhile, for the monolayer, the Berry curvature is not concentratedly localized at the K points [43], i.e., the VBM and CBM in the reciprocal space, which can cause an impure valley Hall effect. In that case, three of the six configurations, I-1, D-2, and D-3, were chosen with their Berry curvatures computed. Here, the Kubo formula approach was utilized, and the Berry curvature was calculated for the entire valence bands. The perturbation method is used to convert the computation of Berry curvatures into a calculation of the interband energy difference, with the expression [66]:

$$\Omega_n(k) = - \sum_{n \neq n'} \frac{2\text{Im} \langle \psi_{nk} | v_x | \psi_{n'k} \rangle \langle \psi_{n'k} | v_y | \psi_{nk} \rangle}{(E_n - E_{n'})^2}, \quad (10)$$

$$\Omega(k) = - \sum_n \sum_{n \neq n'} f_n \frac{2\text{Im} \langle \psi_{nk} | v_x | \psi_{n'k} \rangle \langle \psi_{n'k} | v_y | \psi_{nk} \rangle}{(E_n - E_{n'})^2}, \quad (11)$$

Here, f_n , $E_n(k)$, and $v_{x/y}$ are the Fermi-Dirac distribution function, the eigenvalue of the n -th-band wave function (ψ_{nk}), and the velocity operator, respectively. As illustrated in Fig. 7, due to the K -valley cross-superposition, all K points have a positive value, which can be macroscopically exhibited as a very apparent AHE, where the electrons with the same spin but of different K valleys are biased in one direction. Moreover, due to the intrinsic IS of D-2 and D-3, all six valleys have the same values, while in I-1, the two unequal

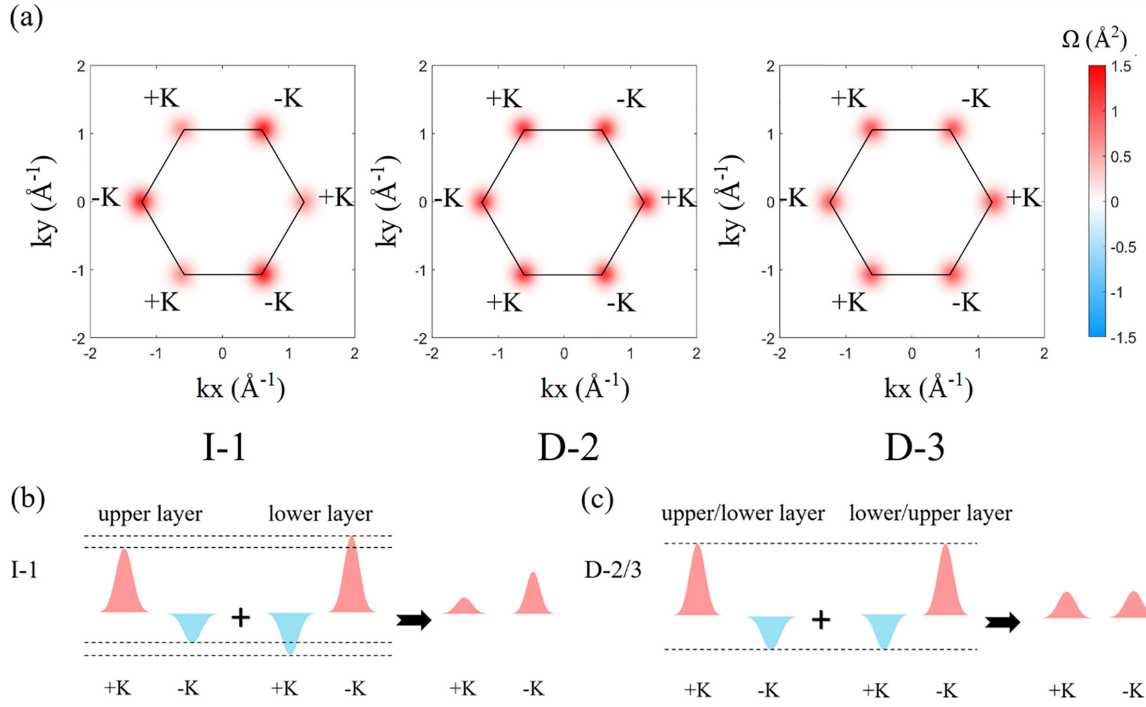


FIG. 8. (a) Berry curvatures of I-1, D-2, and D-3 as a countermap over the two-dimensional (2D) Brillouin zone (BZ) obtained from the derived formula with the fitted results. (b) Schematic diagrams of upper- and lower-layer superpositions of Berry curvatures for (b) I-1 and (c) D-2/3.

k valleys become relatively enlarged and diminished to some extent in magnitude, correspondingly, as a result of breaking both time-IS (TIS) and IS, which is usually achieved by applying external strain in other materials [67,68].

To further understand the difference that occurred at $+K/-K$ valleys, we qualitatively assessed the stacking effect on the AVHE. Since the band dispersion near CBM and VBM are comparably symmetric, we can construct the Hamiltonian in the range of neighborhoods that expanded at six K points in the first BZ by applying the two-band model. Considering the band gap and valley polarization in the band structure, which can respectively be expressed by the second and third terms in the following formula [69]:

$$H = at(\tau k_x \hat{\sigma}_x + k_y \hat{\sigma}_y) + \frac{\Delta}{2} \hat{\sigma}_z - \lambda \hbar \tau (\hat{\sigma}_z - 1) \hat{S}_z, \quad (12)$$

where a is the lattice parameter, t is the equivalent nearest-neighbor hopping term, τ is the valley index, values of ± 1 represent $\pm K$, Δ is the band gap in the case of valley polarization, and $\hat{\sigma}$ with subscripts from x to z are the Pauli matrices. We can derive the following expression (related derivation shown in the Appendix):

$$\Omega_v = \tau \frac{a^2 t^2 \left(\frac{\Delta - \lambda \hbar^2 \tau}{2} \right)}{2 \left[a^2 t^2 k^2 + \left(\frac{\Delta - \lambda \hbar^2 \tau}{2} \right)^2 \right]^{3/2}}. \quad (13)$$

The Berry curvature in the valence band is described by applying the two-band model to characterize the ferrovalley material, a version with SOC as the valley polarization being considered. Based on the formula provided above, the corresponding Berry curvature is illustrated in Fig. 8(a). When $k = 0$, two nondegenerate K valleys with distinct Berry curvature

values are obtained by substituting τ with either $+1$ or -1 . It is observed that the relative size of the energy gaps at these K points is the main contributing factor, as it is inversely proportional to the square of the band gap. Thus, different valleys will exhibit discrepant gap values, corresponding to the Berry curvature deforming away from being equally large and opposite, which is the leading cause of AVHE. Moreover, the band dispersion near CBM and VBM is determined by the energy gap and the type of interlayer coupling, and the latter leads to neglected hopping parameter $t \sim 0.41$ meV, which has a minor impact on the Berry curvature. To determine the Berry curvature of a bilayer system, it is necessary to consider the effects of interlayer coupling, which can result in small energy differences in the band structure, i.e., $\Delta_{\text{upper}} > \Delta_{\text{lower}}$, causing corresponding increases and decreases in the Berry curvatures of the upper and lower layers. The Berry curvature of the bilayer can be determined by adding up the Berry curvatures of the two coupled layers, instead of considering the individual Berry curvatures of the unstacked monolayers, as shown in Fig. 8(b). This suggests that controlling the Berry curvature involves selecting appropriate stacking configurations.

Finally, we focus on evaluating the AHE of the material of particular interest, denoted as I-1, with both valley polarization and concentratedly localized Berry curvatures. We employed the formula:

$$\sigma = -\frac{e^2}{\hbar} \iint_{\text{BZ}} \frac{d^2 k}{(2\pi)^2} \Omega(k), \quad (14)$$

to calculate the anomalous Hall conductivity as a function of energy by integrating the Berry curvature over the BZ [70], as depicted in Fig. 9. Notably, we observed positive values

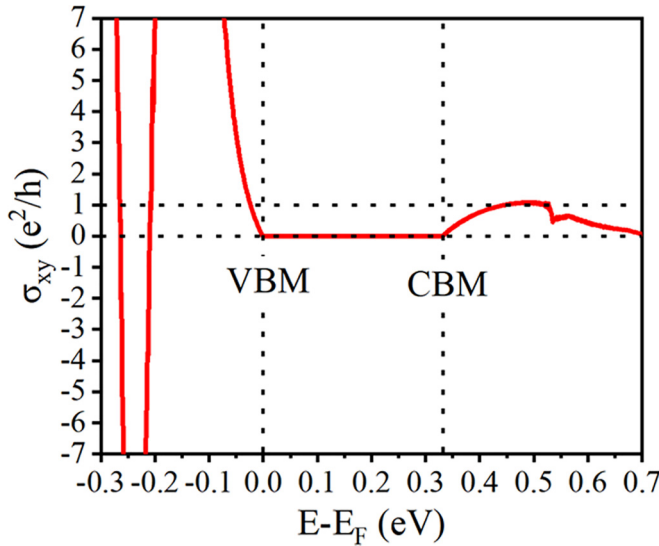


FIG. 9. Anomalous Hall conductivity as a function of energy for I-1.

in the vicinity of both the VBM and CBM, affirming the occurrence of the AHE during electronic transitions in this semiconductor. However, further research is still warranted to elucidate the underlying mechanisms responsible for the observed AHE from experiments and to explore the potential of tuning this effect for specific applications.

IV. CONCLUSIONS

In summary, via first-principles calculations, we found that the designed bilayer VSCI is a direct band gap FM semiconductor that possesses several remarkable properties. These include the complete retention of the sizeable spontaneous valley polarization exhibited by the monolayer, a distinct AVHE, and the generation of spin currents. The peculiarities of the bilayer Janus structure enable a significant energy splitting between its two layers, even in the absence of an external electric field. The computed extremes of the Berry curvature appear at $+K/-K$, and the electrons in the VBM at the $+K/-K$ valleys come from the same spin channel. In this paper, we also provide insight into the physical mechanism behind the

performance differences of the conduction/valence bands and the $+K/-K$ valleys and derived the expression for the Berry curvature of the ferrovalley using the two-band model. Meanwhile, we fitted the computed results to qualitatively assess the origin of the differences in Berry curvature for different stacking configurations. Overall, our work resulted in the design of desirable valleytronics, and we analyzed the outcome to provide ideas for finding more materials.

ACKNOWLEDGMENTS

This paper was supported by the National Natural Science Foundation of China (No. 11904047) and the Natural Science Foundation of Sichuan Province (No. 2022NSFSC1803).

APPENDIX: DERIVATION OF THE TWO-BAND MODEL CONSIDERING SOC

According to the form of Hamiltonian, the eigenvalue, namely, the energy of two bands can be written as

$$E = \frac{\lambda\hbar^2\tau}{2} \pm \sqrt{\left(\frac{\Delta - \lambda\hbar^2\tau}{2}\right)^2 + a^2 t^2 k^2} \quad (\text{A1})$$

When $k = 0$, the VBM and CBM are

$$E_c = \frac{\Delta}{2}, \quad E_v^{+k} = \lambda\hbar^2 - \frac{\Delta}{2}, \quad E_v^{-k} = -\lambda\hbar^2 - \frac{\Delta}{2}. \quad (\text{A2})$$

The wave function corresponding to the valence band can be obtained by solving for the eigenvector:

$$\phi_v = C \begin{pmatrix} -at\tau k_x + iat k_y \\ \frac{\Delta - \lambda\hbar^2\tau}{2} + \sqrt{\left(\frac{\Delta - \lambda\hbar^2\tau}{2}\right)^2 + a^2 t^2 k^2} \end{pmatrix}, \quad (\text{A3})$$

where C is the normalization factor.

The expression in the main text can be obtained according to the definition of Berry curvature:

$$\Omega_v = \nabla \times A, \quad A = -\text{Im}\langle\phi_v|\nabla_k|\phi_v\rangle. \quad (\text{A4})$$

- [1] S. Sharma, P. Elliott, and S. Shallcross, THz induced giant spin and valley currents, *Sci. Adv.* **9**, eadf3673 (2023).
- [2] A. Ciarrocchi, F. Tagarelli, A. Avsar, and A. Kis, Excitonic devices with van der Waals heterostructures: Valleytronics meets twistrionics, *Nat. Rev. Mater.* **7**, 449 (2022).
- [3] J. R. Schaibley, H. Yu, G. Clark, P. Rivera, J. S. Ross, K. L. Seyler, W. Yao, and X. Xu, Valleytronics in 2D materials, *Nat. Rev. Mater.* **1**, 16055 (2016).
- [4] D. Xiao, W. Yao, and Q. Niu, Valley-contrasting Physics in Graphene: Magnetic Moment and Topological Transport, *Phys. Rev. Lett.* **99**, 236809 (2007).
- [5] B. Huang, G. Clark, E. Navarro-Moratalla, D. R. Klein, R. Cheng, K. L. Seyler, D. Zhong, E. Schmidgall, M. A. McGuire, D. H. Cobden *et al.*, Layer-dependent ferromagnetism in a van

der Waals crystal down to the monolayer limit, *Nature (London)* **546**, 270 (2017).

- [6] C. Gong, L. Li, Z. Li, H. Ji, A. Stern, Y. Xia, T. Cao, W. Bao, C. Wang, Y. Wang *et al.*, Discovery of intrinsic ferromagnetism in two-dimensional van der Waals crystals, *Nature (London)* **546**, 265 (2017).
- [7] N. Miao, B. Xu, L. Zhu, J. Zhou, and Z. Sun, 2D intrinsic ferromagnets from van der Waals antiferromagnets, *J. Am. Chem. Soc.* **140**, 2417 (2018).
- [8] P. Jiang, C. Wang, D. Chen, Z. Zhong, Z. Yuan, Z.-Y. Lu, and W. Ji, Stacking tunable interlayer magnetism in bilayer CrI₃, *Phys. Rev. B* **99**, 144401 (2019).
- [9] W.-Y. Tong, S.-J. Gong, X. Wan, and C.-G. Duan, Concepts of ferrovalley material and anomalous valley Hall effect, *Nat. Commun.* **7**, 13612 (2016).

- [10] C.-S. Hu, Y.-J. Wu, Y.-S. Liu, S. Fu, X.-N. Cui, Y.-H. Wang, and C.-W. Zhang, Single-layer intrinsic 2H-phase LuX_2 ($X = \text{Cl}, \text{Br}, \text{I}$) with large valley polarization and anomalous valley Hall effect, *Chin. Phys. B* **32**, 37306 (2023).
- [11] N. Sheremetyeva, I. Na, A. Saraf, S. M. Griffin, and G. Hautier, Prediction of topological phases in metastable ferromagnetic MPX_3 monolayers, *Phys. Rev. B* **107**, 115104 (2023).
- [12] S. Park, S. Arscott, T. Taniguchi, K. Watanabe, F. Sirotti, and F. Cadiz, Efficient valley polarization of charged excitons and resident carriers in molybdenum disulfide monolayers by optical pumping, *Commun. Phys.* **5**, 73 (2022).
- [13] J. Holler, M. Selig, M. Kempf, J. Zipfel, P. Nagler, M. Katzer, F. Katsch, M. V. Ballottin, A. A. Mitioglu, A. Chernikov *et al.*, Interlayer exciton valley polarization dynamics in large magnetic fields, *Phys. Rev. B* **105**, 085303 (2022).
- [14] P. Kapuściński, D. Vaclavkova, M. Grzeszczyk, A. O. Slobodeniuk, K. Nogajewski, M. Bartos, K. Watanabe, T. Taniguchi, C. Faugeras, A. Babiński *et al.*, Valley polarization of singlet and triplet trions in a WS_2 monolayer in magnetic fields, *Phys. Chem. Chem. Phys.* **22**, 19155 (2020).
- [15] T. Smoleński, M. Goryca, M. Koperski, C. Faugeras, T. Kazimierczuk, A. Bogucki, K. Nogajewski, P. Kossacki, and M. Potemski, Tuning Valley Polarization in a WSe_2 Monolayer with a Tiny Magnetic Field, *Phys. Rev. X* **6**, 021024 (2016).
- [16] E. C. Castro, D. S. Brandão, H. Bragança, A. S. Martins, F. Riche, A. C. Dias, J. H. Zhao, A. L. A. Fonseca, and F. Qu, Mechanisms of interlayer exciton emission and giant valley polarization in van der Waals heterostructures, *Phys. Rev. B* **107**, 035439 (2023).
- [17] J. Dang, M. Yang, X. Xie, Z. Yang, D. Dai, Z. Zuo, C. Wang, K. Jin, and X. Xu, Enhanced valley polarization in $\text{WS}_2/\text{LaMnO}_3$ heterostructure, *Small* **18**, 2106029 (2022).
- [18] R. J. Sun, J. J. Lu, X. W. Zhao, G. C. Hu, X. B. Yuan, and J. F. Ren, Robust valley polarization induced by super-exchange effects in HfNX ($X = \text{Cl}, \text{Br}, \text{I}$)/ FeCl_2 two-dimensional ferrovalley heterostructures, *Appl. Phys. Lett.* **120**, 063103 (2022).
- [19] S. Feng, C. Cong, S. Konabe, J. Zhang, J. Shang, Y. Chen, C. Zou, B. Cao, L. Wu, N. Peimyoo *et al.*, Engineering valley polarization of monolayer WS_2 : A physical doping approach, *Small* **15**, 1805503 (2019).
- [20] D. Zhang and B. Zhou, Conduction band-edge valley splitting in two-dimensional ferroelectric AgBiP_2S_6 by magnetic doping: Towards electron valley-polarized transport, *RSC Adv.* **12**, 13765 (2022).
- [21] R. Li, J. Jiang, W. Mi, and H. Bai, Room temperature spontaneous valley polarization in two-dimensional FeClBr monolayer, *Nanoscale* **13**, 14807 (2021).
- [22] C. Li and Y. An, Two-dimensional ferromagnetic semiconductors of rare-earth Janus 2H-GdIBr monolayers with large valley polarization, *Nanoscale* **15**, 8304 (2023).
- [23] K. Sheng, B. Zhang, H.-K. Yuan, and Z.-Y. Wang, Strain-engineered topological phase transitions in ferrovalley 2H- RuCl_2 monolayer, *Phys. Rev. B* **105**, 195312 (2022).
- [24] M. Abdollahi and M. B. Tagani, Janus 2H-VSSe monolayer: Two-dimensional valleytronic semiconductor with nonvolatile valley polarization, *J. Phys.: Condens. Matter* **34**, 185702 (2022).
- [25] W. Pan, Tuning the magnetic anisotropy and topological phase with electronic correlation in single-layer H- FeBr_2 , *Phys. Rev. B* **106**, 125122 (2022).
- [26] R. Peng, T. Zhang, Z. He, Q. Wu, Y. Dai, B. Huang, and Y. Ma, Intrinsic layer-polarized anomalous Hall effect in bilayer MnBi_2Te_4 , *Phys. Rev. B* **107**, 085411 (2023).
- [27] Z.-M. Yu, S. Guan, X.-L. Sheng, W. Gao, and S. A. Yang, Valley-layer Coupling: A New Design Principle for Valleytronics, *Phys. Rev. Lett.* **124**, 037701 (2020).
- [28] T. Zhang, X. Xu, B. Huang, Y. Dai, L. Kou, and Y. Ma, Layer-polarized anomalous Hall effects in valleytronic van der Waals bilayers, *Mater. Horiz.* **10**, 483 (2023).
- [29] L. Wang, Z. Lin, and Y. An, Tunable valley polarization, magnetic anisotropy and dipole moment for layered Janus 2H-VSSe with intrinsic room temperature ferromagnetism, *J. Alloys Compd.* **854**, 157141 (2021).
- [30] N. Zibouche, P. Philippen, A. Kuc, and T. Heine, Transition-metal dichalcogenide bilayers: Switching materials for spintronic and valleytronic applications, *Phys. Rev. B* **90**, 125440 (2014).
- [31] Q. Chen, X. Zheng, P. Jiang, Y.-H. Zhou, L. Zhang, and Z. Zeng, Electric field induced tunable half-metallicity in an A-type antiferromagnetic bilayer LaBr_2 , *Phys. Rev. B* **106**, 245423 (2022).
- [32] W.-Y. Tong and C.-G. Duan, Electrical control of the anomalous valley Hall effect in antiferrovalley bilayers, *npj Quantum Mater.* **2**, 47 (2017).
- [33] T. Zhang, X. Xu, B. Huang, Y. Dai, and Y. Ma, 2D spontaneous valley polarization from inversion symmetric single-layer lattices, *Npj Comput. Mater.* **8**, 64 (2022).
- [34] Y. C. Cheng, Z. Y. Zhu, M. Tahir, and U. Schwingenschlögl, Spin-orbit-induced spin splittings in polar transition metal dichalcogenide monolayers, *Europhys. Lett.* **102**, 57001 (2013).
- [35] A.-Y. Lu, H. Zhu, J. Xiao, C.-P. Chuu, Y. Han, M.-H. Chiu, C.-C. Cheng, C.-W. Yang, K.-H. Wei, Y. Yang *et al.*, Janus monolayers of transition metal dichalcogenides, *Nat. Nanotechnol.* **12**, 744 (2017).
- [36] J. Liang, W. Wang, H. Du, A. Hallal, K. Garcia, M. Chshiev, A. Fert, and H. Yang, Very large Dzyaloshinskii-Moriya interaction in two-dimensional Janus manganese dichalcogenides and its application to realize skyrmion states, *Phys. Rev. B* **101**, 184401 (2020).
- [37] H. Yang, J. Liang, and Q. Cui, First-principles calculations for Dzyaloshinskii-Moriya interaction, *Nat. Rev. Phys.* **5**, 43 (2023).
- [38] C. Zhang, Y. Nie, S. Sanvito, and A. Du, First-principles prediction of a room-temperature ferromagnetic Janus VSSe monolayer with piezoelectricity, ferroelasticity, and large valley polarization, *Nano Lett.* **19**, 1366 (2019).
- [39] Z. Guan and S. Ni, Predicted 2D ferromagnetic Janus VSeTe monolayer with high Curie temperature, large valley polarization and magnetic crystal anisotropy, *Nanoscale* **12**, 22735 (2020).
- [40] Z. Guan and S. Ni, Strain-controllable high Curie temperature, large valley polarization, and magnetic crystal anisotropy in a 2D ferromagnetic Janus VSeTe monolayer, *ACS Appl. Mater. Interfaces* **12**, 53067 (2020).
- [41] Y.-F. Zhao, Y.-H. Shen, H. Hu, W.-Y. Tong, and C.-G. Duan, Combined piezoelectricity and ferrovalley properties in Janus monolayer VCIBr , *Phys. Rev. B* **103**, 115124 (2021).
- [42] W. Liu, X. Li, C. Zhang, and S. Yan, Janus VXY monolayers with tunable large Berry curvature, *J. Semicond.* **43**, 042501 (2022).

- [43] H. Yang, M. Song, Y. Li, Y. Guo, and K. Han, Ferromagnetism and valley polarization in Janus single-layer VS₂, *Physica E* **143**, 115341 (2022).
- [44] P. E. Blöchl, Projector augmented-wave method, *Phys. Rev. B* **50**, 17953 (1994).
- [45] G. Kresse and J. Furthmüller, Efficient iterative schemes for *ab initio* total-energy calculations using a plane-wave basis set, *Phys. Rev. B* **54**, 11169 (1996).
- [46] G. Kresse and J. Hafner, *Ab initio* molecular-dynamics simulation of the liquid-metal–amorphous-semiconductor transition in germanium, *Phys. Rev. B* **49**, 14251 (1994).
- [47] J. P. Perdew, K. Burke, and M. Ernzerhof, Generalized Gradient Approximation Made Simple, *Phys. Rev. Lett.* **77**, 3865 (1996).
- [48] S. Grimme, S. Ehrlich, and L. Goerigk, Effect of the damping function in dispersion corrected density functional theory, *J. Comput. Chem.* **32**, 1456 (2011).
- [49] J. Heyd, G. E. Scuseria, and M. Ernzerhof, Hybrid functionals based on a screened Coulomb potential, *J. Chem. Phys.* **118**, 8207 (2003).
- [50] V. Wang, N. Xu, J.-C. Liu, G. Tang, and W.-T. Geng, VASPKIT: A user-friendly interface facilitating high-throughput computing and analysis using VASP code, *Comput. Phys. Commun.* **267**, 108033 (2021).
- [51] T. Fukui, Y. Hatsugai, and H. Suzuki, Chern numbers in discretized Brillouin zone: Efficient method of computing (spin) Hall conductances, *J. Phys. Soc. Jpn.* **74**, 1674 (2005).
- [52] A. A. Mostofi, J. R. Yates, G. Pizzi, Y.-S. Lee, I. Souza, D. Vanderbilt, and N. Marzari, An updated version of WANNIER90: A tool for obtaining maximally-localised Wannier functions, *Comput. Phys. Commun.* **185**, 2309 (2014).
- [53] H.-U. Kim, H. Seok, W. S. Kang, and T. Kim, The first progress of plasma-based transition metal dichalcogenide synthesis: A stable 1T phase and promising applications, *Nanoscale Adv.* **4**, 2962 (2022).
- [54] S. M. Shinde, K. P. Dhakal, X. Chen, W. S. Yun, J. Lee, H. Kim, and J.-H. Ahn, Stacking-controllable interlayer coupling and symmetric configuration of multilayered MoS₂, *NPG Asia Mater.* **10**, e468 (2018).
- [55] See Supplemental Material at <http://link.aps.org/supplemental/10.1103/PhysRevB.108.075423> for the side view of six stacking configurations before optimization, the phonon spectra of each stacking configuration, and the band structures of each stacking configuration (HSE+SOC).
- [56] A. Togo, L. Chaput, T. Tadano, and I. Tanaka, Implementation strategies in PHONOPY and PHONO3PY, *J. Phys.: Condens. Matter* **35**, 353001 (2023).
- [57] Q. Cui, Y. Zhu, J. Liang, P. Cui, and H. Yang, Spin-valley coupling in a two-dimensional VS₂N₄ monolayer, *Phys. Rev. B* **103**, 085421 (2021).
- [58] Y. Zhu, Q. Cui, Y. Ga, J. Liang, and H. Yang, Anomalous valley Hall effect in A-type antiferromagnetic van der Waals heterostructures, *Phys. Rev. B* **105**, 134418 (2022).
- [59] H. K. Gweon, H.-J. Park, K.-W. Kim, K.-J. Lee, and S. H. Lim, Intrinsic origin of interfacial second-order magnetic anisotropy in ferromagnet/normal metal heterostructures, *NPG Asia Mater.* **12**, 23 (2020).
- [60] D. J. P. de Sousa, M. J. Sammon, R. Kim, H. Li, I. A. Young, and T. Low, Spin torque generated by valley Hall effect in WSe₂, *Phys. Rev. B* **106**, 184412 (2022).
- [61] D. MacNeill, G. M. Stiehl, M. H. D. Guimaraes, R. A. Buhrman, J. Park, and D. C. Ralph, Control of spin-orbit torques through crystal symmetry in WTe₂/ferromagnet bilayers, *Nat. Phys.* **13**, 300 (2017).
- [62] P. Rivera, K. L. Seyler, H. Yu, J. R. Schaibley, J. Yan, D. G. Mandrus, W. Yao, and X. Xu, Valley-polarized exciton dynamics in a 2D semiconductor heterostructure, *Science* **351**, 688 (2016).
- [63] M.-H. Whangbo, H. Xiang, H.-J. Koo, E. E. Gordon, and J. L. Whitten, Electronic and structural factors controlling the spin orientations of magnetic ions, *Inorg. Chem.* **58**, 11854 (2019).
- [64] M.-H. Whangbo, E. E. Gordon, H. Xiang, H.-J. Koo, and C. Lee, Prediction of spin orientations in terms of HOMO-LUMO interactions using spin-orbit coupling as perturbation, *Acc. Chem. Res.* **48**, 3080 (2015).
- [65] M. P. Marder, *Condensed Matter Physics* (John Wiley & Sons, Hoboken, 2010).
- [66] D. J. Thouless, M. Kohmoto, M. P. Nightingale, and M. den Nijs, Quantized Hall Conductance in a Two-Dimensional Periodic Potential, *Phys. Rev. Lett.* **49**, 405 (1982).
- [67] H. Chi, Y. Ou, T. B. Eldred, W. Gao, S. Kwon, J. Murray, M. Dreyer, R. E. Butera, A. C. Foucher, H. Ambaye *et al.*, Strain-tunable Berry curvature in quasi-two-dimensional chromium telluride, *Nat. Commun.* **14**, 3222 (2023).
- [68] J. Son, K.-H. Kim, Y. H. Ahn, H.-W. Lee, and J. Lee, Strain Engineering of the Berry Curvature Dipole and Valley Magnetization in Monolayer MoS₂, *Phys. Rev. Lett.* **123**, 036806 (2019).
- [69] D. Xiao, G.-B. Liu, W. Feng, X. Xu, and W. Yao, Coupled Spin and Valley Physics in Monolayers of MoS₂ and Other Group-VI Dichalcogenides, *Phys. Rev. Lett.* **108**, 196802 (2012).
- [70] Y. Yao, L. Kleinman, A. H. MacDonald, J. Sinova, T. Jungwirth, D.-s. Wang, E. Wang, and Q. Niu, First Principles Calculation of Anomalous Hall Conductivity in Ferromagnetic bcc Fe, *Phys. Rev. Lett.* **92**, 037204 (2004).